







Magnetocaloric behavior and magnetic ordering in MnPdGa

Yuzki M. Oey ^{1,*}, Daniil A. Kitchaev ¹, Joshua D. Bocarsly ¹, Emily C. Schueller ¹,
Joya A. Cooley ² and Ram Seshadri ^{1,3}

¹*Materials Department and Materials Research Laboratory, University of California, Santa Barbara, Santa Barbara, California 93106, United States*

²*Department of Chemistry and Biochemistry, California State University, Fullerton, California 92831, United States*

³*Department of Chemistry and Biochemistry, University of California, Santa Barbara, Santa Barbara, California 93106, United States*



(Received 9 October 2020; accepted 7 January 2021; published 26 January 2021)

MnPdGa, a compound crystallizing in the Ni₂In structure, is a material displaying magnetic ordering near room temperature and is a potential ambient-temperature magnetocaloric. Screening based on electronic structure calculations suggest that MnPdGa may exhibit a high magnetocaloric figure of merit due to its strong magnetostructural coupling. Here we report the preparation of MnPdGa and employ high-resolution synchrotron x-ray diffraction to confirm its hexagonal Ni₂In-type structure. The zero-field ground state is shown to be a conical spin-wave state, defined by a long-range modulation of the conventional conical antiferromagnet structure. Near the Curie temperature, the measurements carried out here coupled with electronic structure calculations suggest that a fully ferromagnetic state can form at elevated temperatures under an applied field. A peak magnetocaloric entropy change $\Delta S_M = -3.54 \text{ J kg}^{-1} \text{ K}^{-1}$ ($30.1 \text{ mJ cm}^{-3} \text{ K}^{-1}$) is measured at $T_C = 315 \text{ K}$ at an applied field $H = 5 \text{ T}$. The exchange-driven, nontrivial magnetic structure found in MnPdGa is compared with the somewhat better-studied MnPtGa on the basis of electronic structure calculations.

DOI: [10.1103/PhysRevMaterials.5.014414](https://doi.org/10.1103/PhysRevMaterials.5.014414)

I. INTRODUCTION

Magnetocalorics recently gained popularity as environmentally safe and efficient refrigerants compared to materials used in traditional vapor compression [1–3]. In a typical ferromagnet, application of a magnetic field when the material is close to the Curie temperature causes the moments to partially align. If this magnetization is performed adiabatically, the lattice entropy increases to compensate the decreased entropy of the spins, raising the temperature of the material. Conversely, when the field is removed, the temperature decreases. By alternating adiabatic and isothermal magnetization and demagnetization steps, a magnetic heat pump can be built in direct analogy to a conventional vapor-compression heat pump. The most common metric used to characterize the strength of a magnetocaloric is $\Delta S_M(T, H)$, the isothermal entropy change at temperature T with an applied magnetic field H . Generally, magnetocalorics are evaluated by the peak value of ΔS_M for a given applied field in gravimetric units $\text{J kg}^{-1} \text{ K}^{-1}$; however, for applications where weight is not as important, the volumetric units $\text{mJ cm}^{-3} \text{ K}^{-1}$ are perhaps of more interest.

For practical use, a magnetocaloric should ideally function in a wide temperature range, but this temperature range is not considered in the ΔS_M figure of merit [4]. Refrigerant capacity (RC) is often considered in addition to ΔS_M when comparing magnetocalorics with a second-order magnetic transition near room temperature. RC is a measure of how much heat is transferred between hot and cold reservoirs, and

is calculated as the area under the ΔS_M curve truncated at the full width at half maximum (FWHM) [3].

A computational proxy based on density-functional-theory-based electronic structure calculations (DFT), the magnetic deformation (Σ_M), has shown promise in predicting magnetocaloric performance in ferromagnets [5,6]. Σ_M estimates the strength of magnetostructural coupling in a material by quantifying the amount of unit cell deformation between DFT-relaxed structures calculated with and without spin polarization. This metric correlates well with ΔS_M in a broad range of materials, including those with first-order magnetostructural transitions and those with continuous transitions [5–8]. Compounds with Σ_M greater than 1.5% indicate a promising candidate, meriting experimental study.

DFT calculations on MnPdGa gave a $\Sigma_M = 2.8\%$, suggesting that this material could be expected to display significant magnetostructural coupling and may be promising for study as a magnetocaloric. MnPdGa has not been very well investigated, with limited magnetic and electronic data reported. Based on powder x-ray and neutron diffraction, it has been characterized as a hexagonal Ni₂In-type ferromagnet with the moments pointing along the c axis [9]. The Curie temperature was found to be around 325 K, but at around 150 K, a second magnetic transition is observed, in which the ferromagnetic (FM) moments tilt away from the c axis to form a canted antiferromagnetic (AFM) structure with a reduced net moment. A more recent study using Lorentz TEM and magnetic measurements suggested that this material may also host biskyrmion phases up to fields of 1.2 T [10].

Here we explore the magnetocaloric response in MnPdGa prepared by arc-melting and characterized using high-resolution synchrotron data to confirm the Ni₂In-type

*yoey@ucsb.edu

hexagonal crystal structure, previously proposed on the basis of powder x-ray and neutron diffraction. We find a magnetocaloric response of $\Delta S_M = -3.54 \text{ J kg}^{-1} \text{ K}^{-1}$ ($-30.1 \text{ mJ cm}^{-3} \text{ K}^{-1}$) for an applied field $H = 5 \text{ T}$ near $T_C = 315 \text{ K}$. While these values are somewhat smaller than anticipated from the computed Σ_M proxy, a significant refrigerant capacity of 224.6 J kg^{-1} was observed. We show that the origin of the reduced magnetocaloric effect as compared to the prediction from ΔS_M is noncollinear magnetic order which has an AFM component in addition to the FM moment. This effect is analogous to the behavior seen in isostructural MnPtGa [11], although the size of the AFM component and reduction in magnetocaloric response is less pronounced in MnPdGa. Finally, we use electronic structure calculations to show that despite the similarities between MnPdGa and MnPtGa, subtle differences in the Mn spin-spin exchange interactions driven by the Pd/Pt substitution lead to substantial differences in the macroscopic magnetic moment, long-range magnetic order, and ultimately magnetocaloric performance.

II. MATERIALS AND METHODS

Polycrystalline ingots of MnPdGa were prepared by arc-melting and furnace annealing elemental Mn (Alfa Aesar, 99.95%), Pd powder (Alfa Aesar, 99.95%), and Ga buttons (Alfa Aesar, 99.9999%) in 0.5 g batches. Pieces of Mn were cleaned by sealing in an evacuated fused silica tube and annealing at 1273 K overnight before use. About 0.010 g excess Mn was used to account for Mn loss via vaporization during arc melting. Cleaned Mn chips were ground into a powder and mixed thoroughly with a stoichiometric quantity of Pd powder, and the mixture was pressed into a 6-mm diameter pellet at 2 metric tons *per* 0.317 cm^2 . This pellet was arc-melted with Ga in an Ar atmosphere, and the ingot was flipped over and remelted twice to ensure homogeneity. The resulting ingot was sealed in an evacuated fused silica tube (7-mm inner diameter) backfilled with 10 psi of Ar and annealed at 1073 K for five days. The sample was quenched in water.

High-resolution synchrotron powder x-ray data were acquired through the mail-in program at the Argonne National Laboratory, Advanced Photon Source (APS) on beamline 11-BM with an average wavelength of $\lambda = 0.457913 \text{ \AA}$. The ingots of the sample were crushed into powder and packed in a kapton capillary (inner diameter 0.8 mm). Data at room temperature (295 K) were acquired between $Q = 1.0 \text{ \AA}^{-1}$ to 11.4 \AA^{-1} with a sample acquisition time of 42 minutes. TOPAS ACADEMIC [12] was used to refine the patterns [13], and crystal structures were visualized using VESTA [14]. For composition analysis, 50 mg of the powder sample was pressed into a 6-mm diameter pellet and three 0.5-mm diameter points on the pellet surface were analyzed using a Rigaku ZSX Primus VI wavelength dispersive x-ray fluorescence (XRF) instrument.

A Quantum Design superconducting quantum interface device (SQUID) magnetic property measurement system (MPMS) with a vibrating sample magnetometer (VSM) was used to take magnetization data on a 5.31-mg piece of sample that was placed into a plastic sample holder and loaded into a brass rod sample holder. Temperature-dependent magnetization data were acquired under a field of $H = 0.1 \text{ T}$ between

10 K and 350 K, under both zero-field-cooled and field-cooled conditions. A magnetization versus field hysteresis loop was acquired at 10 K in a field between 5 T and -5 T . To determine the magnetic entropy change as a function of applied field, $\Delta S_M(H, T)$ was obtained using the Maxwell relation $(\partial M/\partial T)_H = (\partial S/\partial H)_T$, using M versus T measurements taken by sweeping temperature at eight fixed magnetic fields between $H = 0.1 \text{ T}$ and 5 T. The data were analyzed using the `magentro.py` code [15].

Electronic structure calculations on MnPdGa and MnPtGa were performed using DFT as implemented in the Vienna *ab initio* simulation package (VASP) [16] with projector augmented wave (PAW) pseudopotentials [17,18] within the Perdew-Burke-Ernzerhof (PBE) generalized gradient approximation (GGA) [19]. The hexagonal unit cell of MnPdGa was first relaxed in a non-spin-polarized and spin-polarized FM calculations with force convergence of $0.001 \text{ eV \AA}^{-1}$ without spin-orbit coupling. Electronic densities of states (DOS) for each case were calculated for k -point grids of $10 \times 10 \times 8$ and energy convergence criteria of 10^{-5} eV per cell. Calculations for the canted magnetic structures of MnPdGa and MnPtGa were performed within the orthohexagonal cell, increasing the convergence threshold to 10^{-7} eV per cell. In these calculations, the moment directions were constrained to various canting angles between 0° (collinear ferromagnetism) and 90° (collinear antiferromagnetism). No constraints were placed on the moment magnitudes. Spin-wave calculations were performed using the generalized Bloch's theorem approach to implicitly represent the incommensurate spin structure. Because this implicit representation is not applicable for spin-orbit coupling, we report all energies without including spin-orbit effects. However, we confirm that spin-orbit coupling leads to negligible changes in energy compared to the scale of the energy profile of the canted AFM phase or the spin-wave dispersion relation.

III. RESULTS AND DISCUSSION

Compositional analysis on the sample using XRF revealed an average composition of $\text{Mn}_{1.02(2)}\text{Pd}_{1.01(2)}\text{Ga}_{0.963(3)}$ (standard deviations denoted in parentheses), confirming that the sample is very near its stoichiometric formula. MnPdGa has been previously reported to form a Ni₂In-type hexagonal $P6_3/mmc$ (no. 194) structure as shown in Fig. 1 [9,10]. Pd (Wyckoff site $2d$) and Ga (Wyckoff site $2c$) form honeycomb layers in the ab plane that are offset by $1/3$ of the unit cell. The view down the a axis shows that the Pd-Ga substructure alternate with layers of Mn (Wyckoff site $2a$) in the c direction.

Figure 2 shows synchrotron diffraction pattern acquired at 295 K, along with a Rietveld fit to the Ni₂In structure type (space group $P6_3/mmc$). The pattern was fit using the Stephens peak-shape function [20], indicating some anisotropic stain broadening, which is resolvable due to the very high resolution of the synchrotron diffractometer. In addition, some of the peaks show hkl -dependent asymmetry, which was addressed by refining the appropriate asymmetry parameters based on spherical harmonics with three nonzero terms. From the obtained fit, it is clear that all of the peaks in MnPdGa match with the reported Ni₂In structure ($P6_3/mmc$),

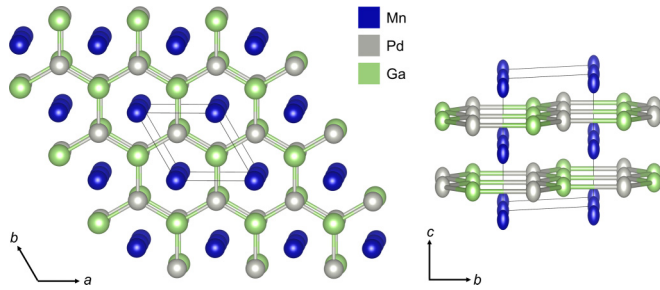


FIG. 1. MnPdGa crystallizes in the hexagonal $P6_3/mmc$ (no. 194) space group. Looking down the c axis, the Pd and Ga make honeycomb lattice layers in the ab plane, with Mn atoms centered between the honeycomb layers. As seen looking down the a axis, the honeycomb layers alternate with layers of Mn on a triangular lattice. The atoms in this view are represented with displacement ellipsoids refined from the synchrotron diffraction data shown at 95% probability.

with no evidence of space-group violations or secondary phases in the sample. In particular, we do not find any evidence of inversion-symmetry breaking as proposed in a recent report on MnPtGa [25]. The small discrepancies that the model has with the data are potentially due to strong absorption of the x-ray beam by the sample.

Temperature- and field-dependent magnetization data are shown in Fig. 3. The M versus T data taken under a constant

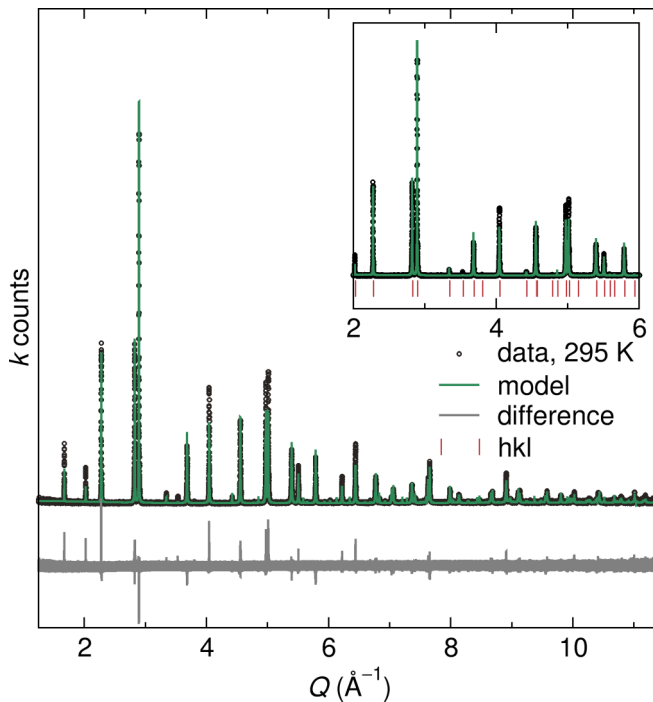


FIG. 2. High-resolution synchrotron x-ray diffraction data acquired at $T = 295$ K fit using Rietveld refinement between $Q = 1.25 \text{ \AA}^{-1}$ to 11.4 \AA^{-1} . MnPdGa crystallizes in the hexagonal $P6_3/mmc$ (no. 194) space group with cell parameters $a = b = 4.34263(3) \text{ \AA}$ and $c = 5.51951(5) \text{ \AA}$, and a volume of $90.147(1) \text{ \AA}^3$. The inset shows hkl positions calculated from $P6_3/mmc$, which line up with all observed peaks.

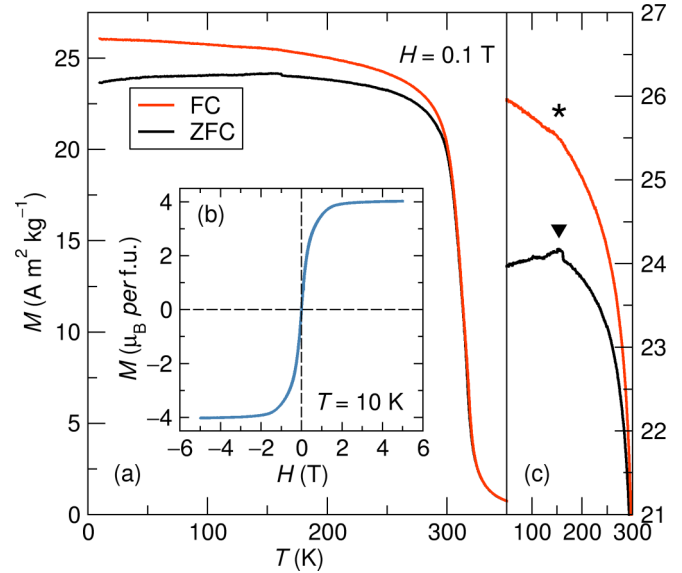


FIG. 3. (a) ZFC and FC temperature-dependent magnetization of MnPdGa taken under a constant field of $H = 0.1$ T. The sample ferromagnetically orders at $T_C = 315$ K and there is an AFM component at around $T_N = 160$ K. (b) Field-dependent magnetization taken at $T = 10$ K between $H = -5$ T and 5 T. (c) Temperature-dependent magnetization around 150 K to 300 K is shown to highlight the AFM component.

field of $H = 0.1$ T reveals that MnPdGa develops FM order at $T_C = 316$ K. This T_C agrees with previous studies of MnPdGa [9,10]. In addition, these studies found a second transition associated with canting of the magnetic moments into a canted AFM state around 140 K [9,10], which we see here at around 160 K in both the ZFC and FC data. The transition is small in the M versus T because it is into a canted state rather than a full AFM state, but agrees with these previous reports which also saw very small inflection changes in the M versus T data. The inset [Fig. 3(b)] shows M versus H at $T = 10$ K, and the saturation moment at 2 T is $94.6 \text{ A m}^2 \text{ kg}^{-1}$ ($3.91 \mu_B$ per f.u.). This moment is much larger than that observed in the MnPtGa under similar conditions ($2.6 \mu_B$ [11] to $3.15 \mu_B$ [21] per f.u.). The shape of this M versus H curve is characteristic of a ferromagnetic material. Canted antiferromagnets also show a similar shape since they have a net moment, so the M versus H data do not discount the canted AFM transition at 160 K. However, the high saturated moment at high field for MnPdGa suggests that the canted AFM moments are aligned back into a FM structure.

To characterize the magnetic entropy change of MnPdGa, M versus T data were taken at eight fields between $H = 0.1$ T and 5 T [Fig. 4(a)]. The derivatives of these data were taken and then integrated to give the ΔS_M curves in Fig. 4(b) according to the formula $\Delta S_M(T, H) = \int_0^H (\partial M) / (\partial T)_{H'} dH'$. The maximum ΔS_M at $H = 5$ T is $-3.54 \text{ J kg}^{-1} \text{ K}^{-1}$. This value is somewhat lower than expected based on the $\Sigma_M = 2.8\%$ prediction. For comparison, MnCoP, with $\Sigma_M = 3.0\%$, shows $\Delta S_M = -6.0 \text{ J kg}^{-1} \text{ K}^{-1}$ [22]. Some of this discrepancy is due to the high density of MnPdGa (8.5 g cm^{-3}), which leads to poor gravimetric performance. In the case of MnPdGa, it may be more useful to compare the volumetric

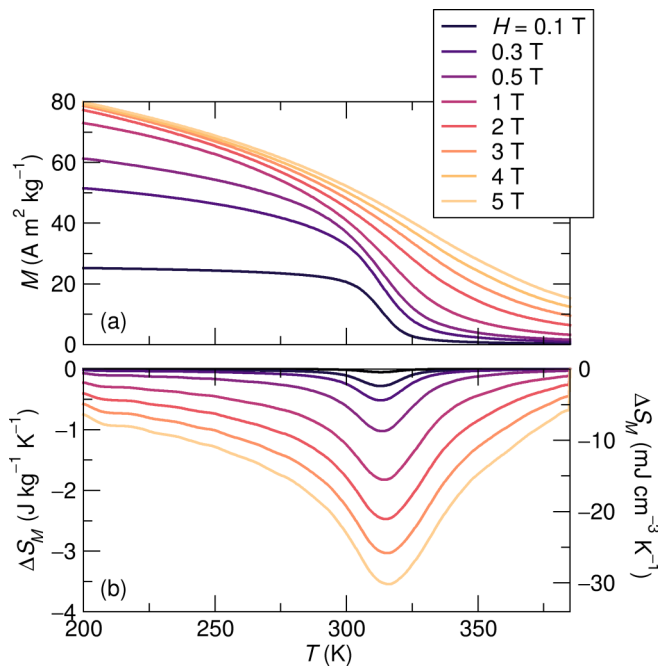


FIG. 4. (a) Temperature-dependent magnetization data were taken at various fields. (b) Derivatives of each curve were taken and integrated to yield ΔS_M . The maximum $-\Delta S_M$ is $3.54 \text{ J kg}^{-1} \text{ K}^{-1}$.

entropy change rather than the gravimetric entropy change with other magnetocalorics. When expressed volumetrically, the ΔS_M of MnPdGa and MnCoP are $30.1 \text{ mJ cm}^{-3} \text{ K}^{-1}$ and $41 \text{ mJ cm}^{-3} \text{ K}^{-1}$, respectively.

In addition, the RC was calculated for MnPdGa using full-width at half-maximum (FWHM). The ΔS_M curves are rather broad, with FWHM temperature span between 266.0 K and 354.5 K for an applied field of 5 T. This results in a large RC of 224.6 J kg^{-1} for an applied field of 5 T. Under a field of $H = 2 \text{ T}$, the FWHM falls between 279.0 K and 338.7 K, with a RC of 85.1 J kg^{-1} . These values are in line for the RC values for many good magnetocalorics, which may be found previously tabulated [3]. Therefore, despite the fairly low gravimetric ΔS_M , the RC calculation suggests that MnPdGa nevertheless may be an interesting magnetocaloric near room temperature.

In MnPtGa, the calculated Σ_M is 2.4%, similar to that of MnPdGa (2.8%). However, a much smaller gravimetric entropy change is observed, with a peak ΔS_M of $-1.9 \text{ J kg}^{-1} \text{ K}^{-1}$ under an applied field $H = 5 \text{ T}$. The heavy Pt again contributes to this low gravimetric entropy change, and the corresponding volumetric entropy change is $-22.3 \text{ mJ cm}^{-3} \text{ K}^{-1}$, more comparable to that of MnPdGa [11].

From these experimental results, it is clear that the magnetocaloric effect in MnPdGa and especially MnPtGa is not as impressive as predicted by Σ_M . The thermodynamic origin of this behavior is that the magnetic structure of both compounds is not purely FM, but includes an AFM component, which accounts for a fraction of the ordering energy. To resolve the precise difference in the magnetic ordering energies of these two compounds, we turn to DFT calculations.

We first characterize the local magnetic structure of both materials by computing the energy profile of possible canted AFM configurations, from the pure FM to the AFM limits. This energy profile is shown in Figs. 5(a) and 5(b) for spin directions alternating along the c and a crystal axes, respectively. The spin-spin interactions along the c -direction are highly nonlinear, reflecting a large contribution of direct exchange within the chain of Mn atoms lying along the c -axis. The optimal local spin configuration is a one-dimensional (1D) chain of canted moments alternating their angle to the c -axis, consistent with the previously proposed canted AFM structure. In both materials, the spins favor a local FM alignment within the (ab) -plane, with an energy profile consistent with a bilinear Heisenberg model. These magnetic energy profiles are negligibly affected by spin-orbit coupling, indicating that this noncollinear itinerant magnetic state arises solely from exchange effects.

Having established the canted AFM structure as the local magnetic ground state, we search for long-range instabilities with respect to the formation of spin waves. While the formation of conventional spin helices is not favorable for any wave vector, we find that conical spin waves can have lower energy than the local canted AFM structure. As shown in Fig. 5(c), these low-energy conical spin waves are defined by a rotation of the canted AFM structure around the crystal c -axis with a propagation wave vector q . The dispersion relation shown in Fig. 5(c) maps the energies of these spin waves for high-symmetry wave vectors. MnPtGa has a single energy minimum corresponding to a spin density wave propagating along the c -axis, consistent with the neutron refinement reported by Cooley *et al.* [11], MnPdGa exhibits two weaker minima, favoring spin waves along the [110] direction in addition to [001]. As with the local canted AFM state, the conical spin wave ground states arise from itinerant exchange effects rather than spin-orbit coupling.

The formation of the canted AFM structure in MnPtGa was previously explained by an instability in the electronic density of states of the FM structure [11]. We find that a similar instability exists in MnPdGa. Figure 6(a) shows the non-spin-polarized DOS, which features a strong peak in the Mn states at the Fermi level, characteristic of a Stoner instability. As in conventional ferromagnets, this instability can be relieved by the introduction of spin-polarization into the electronic structure, as shown in Fig. 6(b). In the FM state, the large peak in Mn states at the Fermi level is split into an occupied peak in the majority spin states below the Fermi level, and an unoccupied peak in the minority spin states above the Fermi level, lowering the energy of the system. However, a small peak at the Fermi level persists in the minority spin states of the FM DOS. Formation of the lower symmetry noncollinear canted magnetic state eliminates the peak at the Fermi level and further lowers the energy of the system [Fig. 6(c)].

The results of our DFT analysis compare favorably with the experimental picture of MnPdGa and MnPtGa and suggest several explanations for the difference in their behaviors. Previous neutron studies of these materials proposed that, upon cooling through T_C , both materials form a FM phase, which transforms into a canted AFM phase at $T_N < T_C$. Cooley *et al.* [11] showed that, upon further cooling, the canted AFM phase in MnPtGa develops a long-wavelength modulation along the

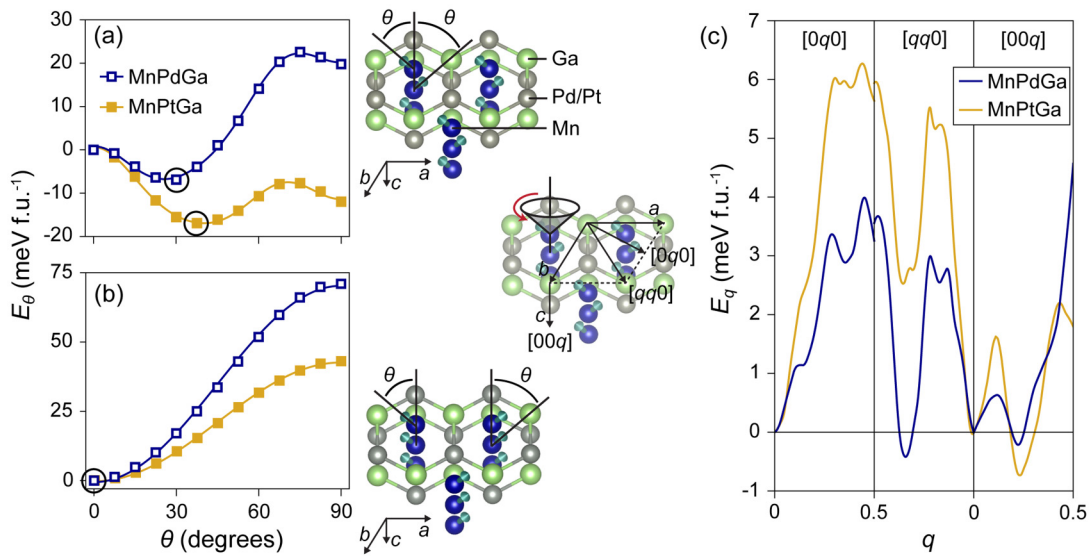


FIG. 5. Computational comparison of the short- and long-range magnetic structures in MnPdGa and MnPtGa. (a, b) Energy of the canted AFM phase as a function of canting angle θ , where the spins alternate canting directions along (a) the c -direction or (b) the a -direction. (c) Energy of conical spin waves defined by a rotation of the locally optimal (a) canted AFM phase around the c -axis, with propagation wave vector q .

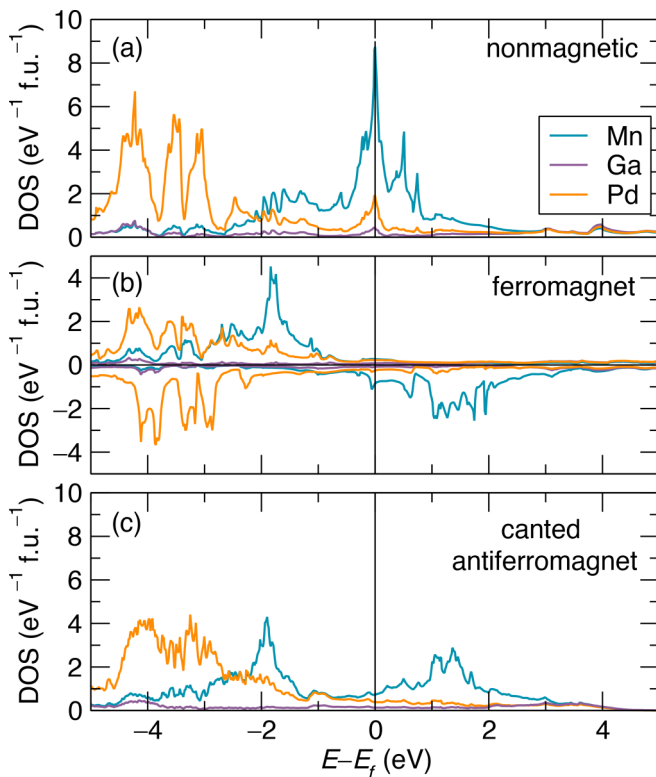


FIG. 6. Electronic density of states (DOS) for MnPdGa with different magnetic structures. (a) The DOS with no spin-polarization. (b) Collinear FM state. States are split into majority spin states (shown as positive DOS) and minority spin states (shown as negative DOS). (c) The lowest energy calculated canted magnetic state (see Fig. 5 for a depiction of the structure). All states are shown in the same spin channel.

c -axis, forming a low- T spin-density wave consistent with the conical spin-wave structure shown in Fig. 5(c). An analogous phase was not observed so far in MnPdGa [9]. Our DFT results indicate that, while the formation of conical spin waves is favorable in both chemistries, there is a single strong minimum in the MnPtGa dispersion relation, as compared to four weak minima for MnPdGa. Thus, MnPtGa is more likely than MnPdGa to form coherent spin waves with a single q -vector, and retain this order at elevated temperatures. Note that none of these spin-wave structures explain the possible formation of biskyrmion magnetic textures in MnPdGa, which have much larger wavelength and are more likely to be caused by structural symmetry breaking and an associated emergence of Dzyaloshinskii-Moriya interactions [23–25].

In relation to magnetocaloric behavior, the critical distinction between these two materials is the greatly diminished saturation moment in MnPtGa as compared to MnPdGa. At low T , the energy scale of the canted AFM phase shown in Fig. 5(a) is large enough that at all experimentally relevant fields, both materials will locally maintain the canted AFM structure and resist field polarization. However, the fully AFM state is a low-energy local minimum in MnPtGa, and nearly a global maximum in MnPdGa. This energy profile means that AFM domain walls are metastable in MnPtGa, resistant to annealing or elimination under applied field. We speculate that this stability of domain walls is responsible for the diminished macroscopic moment seen in MnPtGa at low- T [26], rather than a substantial difference in the partially AFM local spin structure. At temperatures approaching T_C , an additional relevant feature of the energy profile in Fig. 5(a) is the relative energy of the FM state ($\theta = 0$) as compared to other spin configurations. In MnPdGa, the FM state is substantially lower in energy than in MnPtGa, suggesting that this material

is more susceptible to polarization by applied field, once again yielding an enhanced macroscopic magnetization.

IV. CONCLUSION

High-resolution synchrotron data confirms that MnPdGa crystallizes in the hexagonal $P6_3/mmcNi_2In$ -type structure. Despite a significant DFT-predicted Σ_M , the magnetocaloric properties of MnPdGa have thus far not been reported. MnPdGa displays a modest ΔS_M but a significant volumetric entropy change, and the RC calculated at FWHM shows that it may be a promising magnetocaloric material. The broad transition that we see may be improved by annealing the sample at a different temperature, and other work on MnPdGa suggest that varying the Mn to Pd ratio could have interesting effects on the FM transition [9]. Furthermore, although magnetostructural coupling was not confirmed in this study, the low saturation magnetization yet significant RC indicates that magnetostructural coupling may contribute to the magnetocaloric effect in MnPdGa. DFT calculations reveal that canted and conical spin-wave spin structures are favorable in MnPdGa, but less so than in MnPtGa, explaining the improvement in the magnetocaloric figure of merit between MnPtGa and magnetocaloric performance in MnPdGa.

ACKNOWLEDGMENTS

This work was supported by the National Science Foundation (NSF) through DMR 1710638. Partial support from the NSF Materials Research Science and Engineering Center (MRSEC) at UC Santa Barbara DMR 1720256 (IRG-1) is gratefully acknowledged. The research reported here made use of shared facilities of the NSF MRSEC at UC Santa Barbara, which is a member of the Materials Research Facilities Network (www.mrfln.org). Use of the Advanced Photon Source at Argonne National Laboratory was supported by the U.S. Department of Energy, Office of Science, Office of Basic Energy Sciences, under Contract No. DE-AC02-06CH11357. Computational resources for this project were provided by the National Energy Research Scientific Computing Center, a DOE Office of Science User Facility supported by the Office of Science of the US Department of Energy under Contract No. DE-AC02-05CH11231, as well as the Center for Scientific Computing at UC Santa Barbara, which is supported by the National Science Foundation (NSF) Materials Research Science and Engineering Centers program through NSF No. DMR 1720256 and NSF No. CNS 1725797. Y.M.O. and J.D.B. are supported by the National Science Foundation Graduate Research Fellowship Program under Grant No. DGE-1650114.

-
- [1] G. Brown, *J. Appl. Phys.* **47**, 3673 (1976).
 - [2] V. K. Pecharsky and K. A. Gschneidner, Jr., *Phys. Rev. Lett.* **78**, 4494 (1997).
 - [3] V. Franco, J. Blázquez, J. Ipus, J. Law, L. Moreno-Ramírez, and A. Conde, *Prog. Mater. Sci.* **93**, 112 (2018).
 - [4] V. Franco, J. M. Borrego, C. Conde, A. Conde, M. Stoica, and S. Roth, *J. Appl. Phys.* **100**, 083903 (2006).
 - [5] J. D. Bocarsly, E. E. Levin, C. A. Garcia, K. Schwennicke, S. D. Wilson, and R. Seshadri, *Chem. Mater.* **29**, 1613 (2017).
 - [6] C. A. C. Garcia, J. D. Bocarsly, and R. Seshadri, *Phys. Rev. Mater.* **4**, 024402 (2020).
 - [7] Y. M. Oey, J. D. Bocarsly, D. Mann, E. E. Levin, M. Shatruk, and R. Seshari, *Appl. Phys. Lett.* **116**, 212403 (2020).
 - [8] J. D. Bocarsly, E. E. Levin, S. A. Humphrey, T. Faske, W. Donner, S. D. Wilson, and R. Seshadri, *Chem. Mater.* **31**, 4873 (2019).
 - [9] H. Shiraishi, T. Hori, N. Ohkubo, K. Ohoyama, and Y. Yamaguchi, *J. Appl. Phys.* **93**, 6996 (2003).
 - [10] X. Xiao, L. Peng, X. Zhao, Y. Zhang, Y. Dai, J. Guo, M. Tong, J. Li, B. Li, W. Liu, J. Cai, B. Shen, and Z. Zhang, *Appl. Phys. Lett.* **114**, 142404 (2019).
 - [11] J. A. Cooley, J. D. Bocarsly, E. C. Schueller, E. E. Levin, E. E. Rodriguez, A. Huq, S. H. Lapidus, S. D. Wilson, and R. Seshadri, *Phys. Rev. Mater.* **4**, 044405 (2020).
 - [12] A. A. Coelho, *J. Appl. Crystallogr.* **51**, 210 (2018).
 - [13] G. W. Stinton and J. S. Evans, *J. Appl. Crystallogr.* **40**, 87 (2007).
 - [14] K. Momma and F. Izumi, *J. Appl. Crystallogr.* **44**, 1272 (2011).
 - [15] J. D. Bocarsly, R. F. Need, R. Seshadri, and S. D. Wilson, *Phys. Rev. B* **97**, 100404(R) (2018).
 - [16] G. Kresse and J. Furthmüller, *Phys. Rev. B* **54**, 11169 (1996).
 - [17] P. E. Blöchl, *Phys. Rev. B* **50**, 17953 (1994).
 - [18] G. Kresse and D. Joubert, *Phys. Rev. B* **59**, 1758 (1999).
 - [19] J. P. Perdew, K. Burke, and M. Ernzerhof, *Phys. Rev. Lett.* **77**, 3865 (1996).
 - [20] P. W. Stephens, *J. Appl. Crystallogr.* **32**, 281 (1999).
 - [21] K. Buschow and P. van Engen, *Phys. Status Solidi A* **76**, 615 (1983).
 - [22] E. E. Levin, J. D. Bocarsly, J. H. Grebenkemper, R. Issa, S. D. Wilson, T. M. Pollock, and R. Seshadri, *APL Mater.* **8**, 041106 (2020).
 - [23] D. A. Kitchaev, I. J. Beyerlein, and A. Van der Ven, *Phys. Rev. B* **98**, 214414 (2018).
 - [24] E. C. Schueller, D. A. Kitchaev, J. L. Zuo, J. D. Bocarsly, J. A. Cooley, A. Van der Ven, S. D. Wilson, and R. Seshadri, *Phys. Rev. Materials* **4**, 064402 (2020).
 - [25] A. K. Srivastava, P. Devi, A. K. Sharma, T. Ma, H. Deniz, H. L. Meyerheim, C. Felser, and S. S. P. Parkin, *Adv. Mater.* **32**, 1904327 (2020).
 - [26] I. Mazin and M. Johannes, *Nat. Phys.* **5**, 141 (2009).